SCIENTIFIC REP**O**RTS

Mechanochemical synthesis of Si/Cu₃Si-based composite as negative electrode materials for lithium ion battery

Shang-Chieh Hou[1], Tsan-Yao Chen[2], Yu-Hsien Wu[3], Hung-Yuan Chen[3], Xin-Dian Lin[3], Yu-Qi Chen[3], Jow-Lay Huang[1,4,5] & Chia-Chin Chang[3,5]

Mechanochemical synthesis of Si/Cu₃Si-based composite as negative electrode materials for lithium ion battery is investigated. Results indicate that CuO is decomposed and alloyed with Si forming amorphous Cu-Si solid solution due to high energy impacting during high energy mechanical milling (HEMM). Upon carbonization at 800 °C, heating energy induces Cu₃Si to crystallize in nanocrystalline/amorphous Si-rich matrix enhancing composite rigidity and conductivity. In addition, residual carbon formed on outside surface of composite powder as a buff space further alleviates volume change upon lithiation/delithiation. Thus, coin cell made of C-coated Si/Cu₃Si-based composite as negative electrode (active materials loading, 2.3 mg cm^{-2}) conducted at 100 mA g^{-1} performs the initial charge capacity of 1812 mAh g^{-1} (4.08 mAh cm^{-2}) columbic efficiency of 83.7% and retained charge capacity of 1470 mAh g^{-1} (3.31 mAh cm^{-2}) at the end of the 100th cycle, opening a promised window as negative electrode materials for lithium ion batteries.

Rechargeable lithium-ion batteries (LIBs) has been attracted much attention on energy storage due to its high energy density and long cycle life for increasing demand of portable electric devices, electric vehicles (EV), hybrid electric vehicles (HEV), plug-in hybrid electric vehicles (PHEV) and grid energy storage system[1–3]. However, traditional graphite negative material is limited by its theoretical specific capacity of 372 mAh g^{-1}. Thus, a lot of effort are paid to develop next generation materials for negative electrode for LIBs. Silicon is considered to be next generation anode material in lithium ion battery due to its high theoretical specific capacity of 4200 mAh g^{-1}[4], low discharge voltage (~0.4 V versus Li$^+$/Li), highly abundant resource and low toxicity. However, its huge volume change (>400%) during the lithiation/delithiation results in silicon crumbling and pulverizing, leading to loss of integration of the anode[5]. As a result, silicon negative electrode suffers from more irreversible loss, rapid fading of capacity and short cycle life.

The strategies on improving silicon-based anode materials have been conducted including: (i) silicon nanostructure[6–8] such as nanoparticles, nanowires, nanotubes, and porous silicon, (ii) silicon composite such as silicon/active[9] and silicon/inactive composites[10], (iii) novel silicon architecture such as core/shell[11], core/hollow/shell[12]. (iv) electrolyte additives[13] and (v) synthesis of new binders[14].

Silicon-based composites (silicon/active and silicon/inactive) have been widely studied as buffer space, strength and conductivity enhancement to accommodate volume change upon alloying/dealloying and improve intrinsic low conductivity of silicon. Recently, several works have been published utilizing Cu/copper silicide in silicon-based composites as negative electrode materials in LIBs due to its better conductivity and rigidity compared with silicon[15–21]. As compared to sophisticated synthesis, mechanochemical reaction induced by high energy mechanical milling (HEMM) is known as a robust method conventionally employed in mass-production.

[1]Department of Materials Science and Engineering, National Cheng Kung University, Tainan, 70101, Taiwan. [2]Department of Engineering and System Science, National Tsing Hua University, Hsinchu, 30013, Taiwan. [3]Department of Greenergy, National University of Tainan, Tainan, 70005, Taiwan. [4]Center for Micro/Nano Science and Technology, National Cheng Kung University, Tainan, 70101, Taiwan. [5]Hierarchical Green-Energy Materials (Hi-GEM) Research Center, National Cheng Kung University, Tainan, 70101, Taiwan. Correspondence and requests for materials should be addressed to J.-L.H. (email: jlh888@mail.ncku.edu.tw) or C.-C.C. (email: ccchang@mail.nutn.edu.tw)
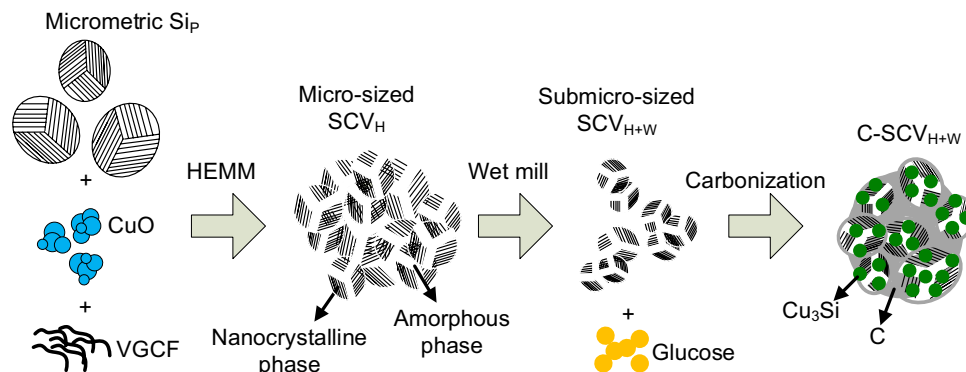
Figure 1. Schematic illustration of the synthesis for Si/Cu$_3$Si-based composite powder.

HEMM reduce powder size, induce crystallite amorphizing and enable alloying reaction under non-equilibrium driven by high mechanical energy[22]. In our previous work, submicro-sized Si aggregate of nanocrystalline/amorphous phases prepared by combining HEMM with wet milling treatments improve Si negative electrode performance[23]. In this work, Cu$_3$Si compound is further synthesized by mechanochemical reaction between CuO and Si upon HEMM. Resulted Cu$_3$Si is embedded and dispersed into nanocrystalline/amorphous Si-rich matrix to fabricate Si/Cu$_3$Si-based composite. Following, carbonization using glucose as carbon source on composite enhances Cu$_3$Si nanocrystallite regardless of nanocrystalline/amorphous Si-rich matrix. Furthermore, residual carbon on composite surface accommodates volume expansion to further improve cycling stability of electrode. Conveniently, both mechanochemical reaction and carbonization are robustly conducted under solid-state condition.

Results

Figure 1 illustrates the synthesis for Si/Cu$_3$Si-based composite powder. First, Mixture of micrometric Si$_P$, CuO and VGCF was high energy mechanically milled to reduce particle size, which induces amorphizing to form micro-sized SCV$_H$ aggregate (nanocrystalline/amorphous phases)[23]. Meanwhile, high energy impacting supposedly leads CuO to decomposing and alloying with Si to form amorphous Cu-Si solid solution. Then, SCV$_H$ was wet milled in ethanol to get submicro-sized SCV$_{H+W}$ aggregate. Finally, carbonization using glucose as carbon source at 800 °C, heating energy enabled Cu$_3$Si to crystallize from Si-Cu solid solution, resulting in Cu$_3$Si distributing into nanocrystalline/amorphous Si-rich matrix for C-SCV$_{H+W}$ aggregate. Besides, residual carbon was covered on surface of C-SCV$_{H+W}$ as buffer layer.

Powder morphology and TGA analyses. Figure 2 shows the SEM images of Si$_P$, SCV$_H$, SCV$_{H+W}$ and C-SCV$_{H+W}$. Micrometric Si$_P$ presents in irregular flake-like shape (Fig. 2(a)). Upon HEMM, Si$_P$, CuO and VGCF are repeatedly fractured and welded to form micro-sized SCV$_H$ aggregate constructed by nano-sized primary particles (Fig. 2(b)). SCV$_H$ is further reduced to submicro-sized SCV$_{H+W}$ after wet milling in ethanol (Fig. 2(c)). After pyrolysis, C-SCV$_{H+W}$ seems to be slightly adhered via residual carbon due to carbonization of glucose on surface (Fig. 2(d)). Supplementary Fig. S1 presents the SEM-EDS spectrum, revealing that C-SCV$_{H+W}$ is consisted of 75.0 wt.% Si, 10.1 wt.% Cu, 5.3 wt.% C, and 9.6 wt.% O. The detected O could be ascribed to the amorphous SiO$_2$ layer on the surface of Si/Cu$_3$Si-based composite particles. More detailed observation using transmission electron microscope (TEM) is shown in Fig. 3(a–c) for SCV$_{H+W}$ and Fig. 3(d–g) for C-SCV$_{H+W}$, respectively. Figure 3(a) and (b) present typical submicro-sized SCV$_{H+W}$ and its selected-area electron diffraction (SAED) pattern, SAED 1 corresponding to (111), (220) and (331) of Si without existing others crystalline phases. Figure 3(c) shows the high-resolution transmission electron microscopy (HRTEM) image indexed as pink circle in Fig. 3(a), demonstrating that SCV$_{H+W}$ is constructed by amorphous laminar welds surrounding the nanocrystalline domain of 0.31 nm d-spacing, corresponding to the (111) planes of Si. In contrast, after carbonization, C-SCV$_{H+W}$ presents darker spots that are embedded and dispersed in Si-rich matrix as blue dash line circle indexed in Fig. 3(d). High-angle annular dark-field imaging and line scan of energy dispersive X-ray spectrometry (EDS) reveal that spot areas are highly concentrated by Cu element, suggesting the exhibition of Cu$_3$Si as shown in Fig. 3(e). Besides the Si pattern, SAED 2 further confirms the electron diffraction pattern for Cu$_3$Si, corresponding to (300) plane as shown in Fig. 3(f). It is consistent with observation of XRD pattern. Figure 3(g) shows the HRTEM image as pink circle indexed in Fig. 3(d), indicating the outside surface of C-SCV$_{H+W}$ is covered by residual carbon originated from glucose carbonization and the inside core of C-SCV$_{H+W}$ is constructed by amorphous/nanocrystalline phases. Therefore, the construction of C-SCV$_{H+W}$ composite could be depicted as the aggregate that nanocrystalline Cu$_3$Si disperses in nanocrystalline/amorphous Si-rich matrix. In addition, among these aggregates are associated via residual carbon. Thermogravimetric analysis (TGA) under air atmosphere for C-SCV$_{H+W}$ is shown in Supplementary Fig. S2. The weight of C-SCV$_{H+W}$ is drastically decreased with temperature from 380 °C to 550 °C, which could be ascribe to the weight loss (~4.7 wt%) of residual carbon. After 550 °C, weight of C-SCV$_{H+W}$ is increased with temperature due to Si oxidation.
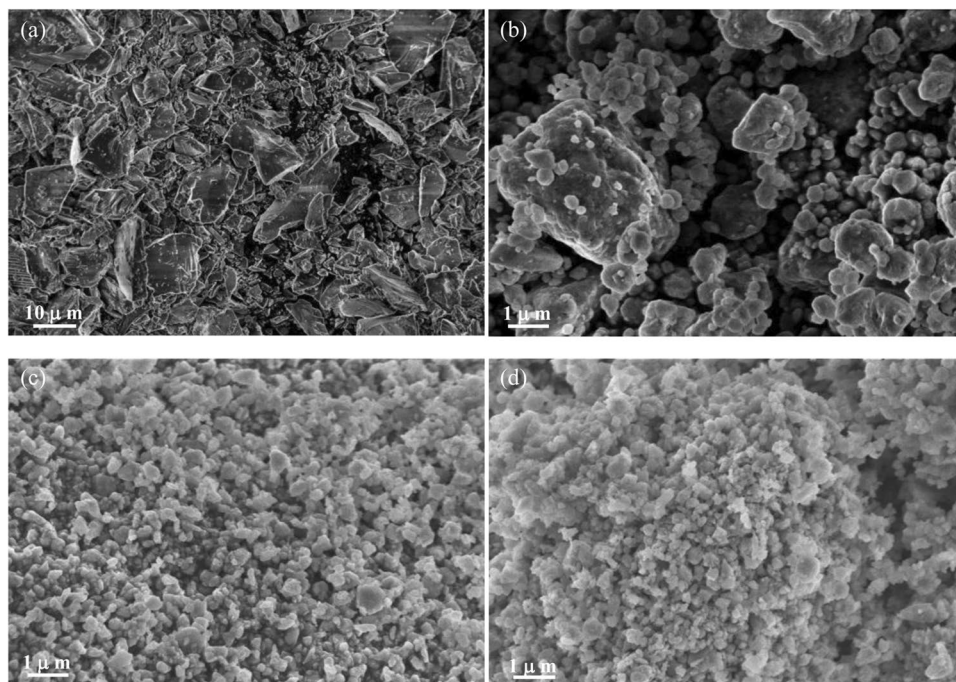
Figure 2. SEM micrographs of the (**a**) Si_P, (**b**) SCV_H, (**c**) SCV_{H+W}, and (**d**) $C\text{-}SCV_{H+W}$, respectively.

**Powder crystalline, XPS and ATR-FTIR analyses.** XRD patterns of the CuO, Si_P, SCV_H, SCV_{H+W} and $C\text{-}SCV_{H+W}$ powders for 2 theta from 10 to 90 degree are shown in Fig. 4. CuO presents peaks (JCPDS card No. 48-1548) at 35.5°, 38.7°, 48.7°, 61.5° and 66.2° (Fig. 4(a)). As well, Si_P demonstrates peaks (JCPDS card No. 65-1060), indexing to (111) at 28.4°, (220) at 47.3°, (311) at 56.1° and (422) at 88.0° (Fig. 4(b)). After high energy mechanical milling for mixture of CuO, Si_P and VGCF, the micro-sized SCV_H shows the broaden peaks similar as Si_P without observation of peaks of CuO. CuO in the SCV_H composite is suspected to decompose and form amorphous Cu-Si solid solution due to high energy impacting upon HEMM (Fig. 4(c)). Followed by moderate wet milling, submicro-sized SCV_{H+W} (Fig. 4(d)) shows no significant difference from micro-sized SCV_H in XRD pattern. After pyrolysis at 800 °C for $C\text{-}SCV_{H+W}$, Cu_3Si peaks (JCPDS card No. 51-0916) indexed to (300) at 45.0° and (012) at 44.6° appear as shown in Fig. 4(e). The average crystallite size of Si calculated by the Scherrer formula from XRD patterns for SCV_{H+W} and $C\text{-}SCV_{H+W}$ is 21 nm and 23 nm, respectively. It implies that heat energy enhances crystalline Cu_3Si formation and slightly increases domain size of Si.

The surface composition for Si_P, SCV_H, SCV_{H+W} and $C\text{-}SCV_{H+W}$ powders is analyzed by X-ray photoelectron spectroscopy (XPS). Figure 5 demonstrates deconvoluted Si2p spectra fitted with five oxidation states with binding energy of 99.2, 100.2, 101.3, 102.1 and 103.4 eV for Si^0, Si^+, Si^{2+}, Si^{3+} and Si^{4+}, respectively[24,25]. Summary of concentrations by integrating the peak intensities for the Si oxidation states of Si2p spectra is shown in Table 1. In all samples as shown in Fig. 5(a–d), the first peak occurring at around 99 eV is assigned to bulk silicon, corresponding to Si^0. Another peak occurring at around 103 eV is ascribed to SiO_2, corresponding to Si^{4+}. Compared to Si_P, SCV_H, SCV_{H+W} and $C\text{-}SCV_{H+W}$ show the peak shifting to lower binding energy from 103.0 eV to 102.5 eV. It might be attributed to mechanochemical reaction between CuO and Si upon HEMM resulting in formations of copper silicide and silicon oxide. As compared to Si_P, $Cu2p_{3/2}$ peak located around 932.8 eV is observed for SCV_H, SCV_{H+W} and $C\text{-}SCV_{H+W}$ (Fig. 5(e)). The binding energy of Cu^{2+} (CuO) located around 934.0 eV shifts to lower binding energy around 932.8 eV, suggesting CuO is reduced[26,27] upon HEMM.

Herein, Si/Cu_3Si-based composite is synthesized by solid-state reaction combining HEMM with heat treatment of carbonization at 800 °C. The sequence is proposed as following reaction (1) and reaction (2). First, CuO is reduced to Cu by Si upon HEMM due to high energy impacting (reaction (1))[28]. Simultaneously, embryo Cu could diffuse into amorphous Si (reaction (2))[29] in excess nanocrystalline/amorphous Si-rich matrix. Followed by carbonization, heat energy further enhance the crystallinity of Cu_3Si. Otherwise, silicon oxide seems to exist in shape of amorphous even after heat treatment at 800 °C for $C\text{-}SCV_{H+W}$.

$$2CuO + Si \rightarrow 2Cu + SiO_2 \qquad (1)$$

$$3Cu + Si \rightarrow Cu_3Si \qquad (2)$$
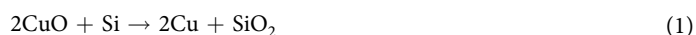
ATR-IR spectra of glucose, Si_P, SCV_H, SCV_{H+W} and $C\text{-}SCV_{H+W}$ present in Fig. 6. The broad band between 1025 and 1257 cm^{-1} can be assigned to Si–O–Si asymmetric stretching and 800 cm^{-1} to Si–O symmetric stretching band, respectively, revealing oxide layer on the surface of these samples. Compared with Si_P, SCV_H and SCV_{H+W} exhibits peak around 966 cm^{-1}, assigning to Si–O–H deformation vibration. It might be ascribed to adsorption of
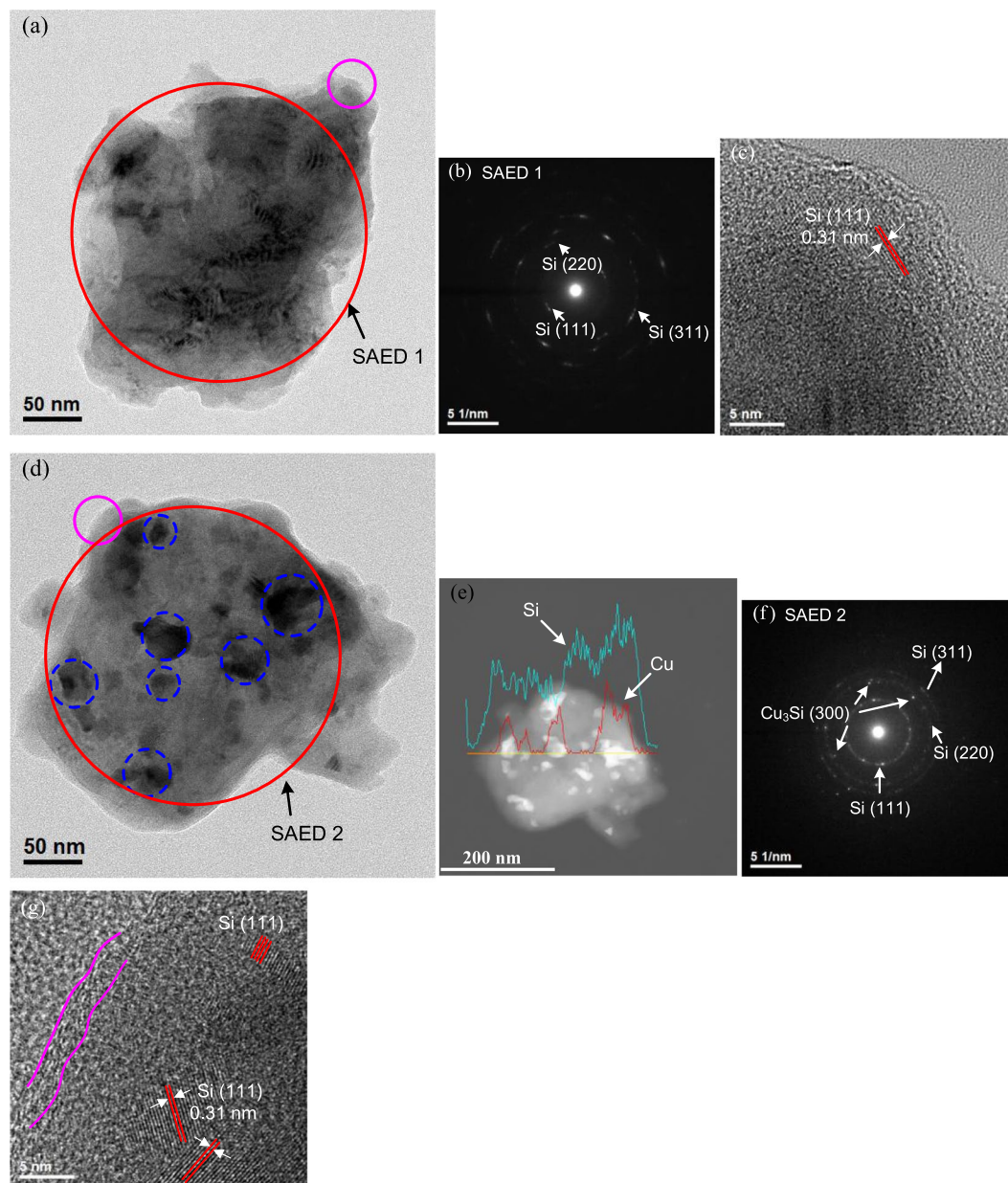
Figure 3. (**a**) TEM image of SCV$_{H+W}$ aggregate, (**b**) SAED 1 pattern, (**c**) HRTEM image referred to pink cycle in (**a**), (**d**) TEM image of C-SCV$_{H+W}$ aggregate, (**e**) corresponding high-angle annular dark-field image of (**d**), (**f**) SAED 2 pattern and (**g**) HRTEM image referred to pink cycle in (**d**).

H$_2$O from ambient surroundings by highly reactive dangling bonds on Si surface attributed to HEMM[30]. SCV$_{H+W}$ presents the symmetric stretching vibration of C–O bond[31–33] after wet milling in ethanol, suggesting that ethanol might be modified on the surface of SCV$_{H+W}$. After carbonization for C-SCV$_{H+W}$, Si–O–H and C–O peaks decrease but Si–O peak around 800 cm^{-1} becomes more significant than Si$_P$, SCV$_H$ and SCV$_{H+W}$.

Electrochemical behavior. Voltage vs. capacity for coin cells with negative electrodes of SCV$_H$, SCV$_{H+W}$ and C-SCV$_{H+W}$ in the 1st and 2nd lithiation/delithiation cycle are shown in Fig. 7(a) and (b), respectively. In the lithiation/delithiation cycles, current density is 200 mA g^{-1} and voltage is ranged between 0.002 V and 1.5 V at room temperature. In the first cycle, initial specific charge (delithiation) capacities is 2273 mAh g^{-1} for SCV$_H$, 2264 mAh g^{-1} for SCV$_{H+W}$ and 1671 mAh g^{-1} for C-SCV$_{H+W}$. Columbic efficiencies of the three negative electrodes in the first cycle are 86.9%, 83.2%, and 83.2%, respectively. C-SCV$_{H+W}$ performs distinguished lithiation from SCV$_H$ and SCV$_{H+W}$, existing a steep potential drop from 1.5 to 0.06 V vs. Li/Li$^+$ (0 to ~200 mAh g^{-1}) in the first cycle. It could be attributed to recovery of crystallite size for Si (i.e. 21 nm and 23 nm for SCV$_{H+W}$ and C-SCV$_{H+W}$, respectively) and residual carbon coating derived from glucose carbonization on C-SCV$_{H+W}$ surface, resulting in various SEI formations.
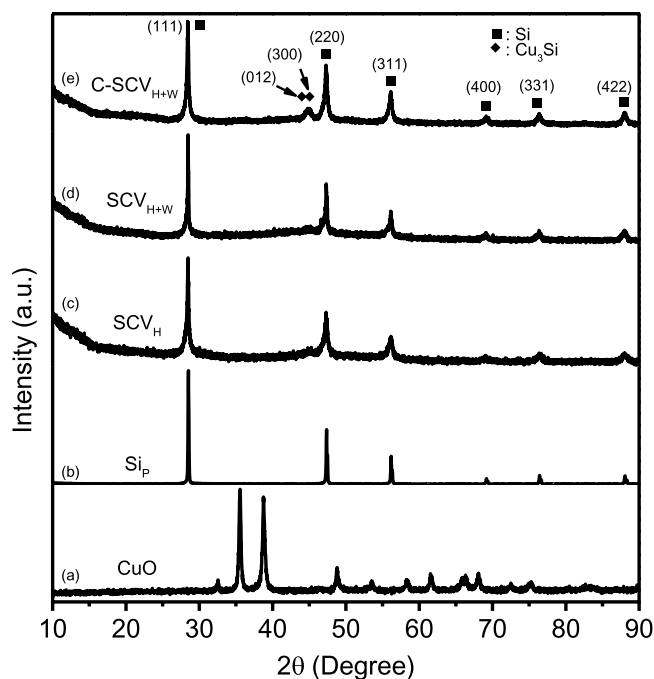
Figure 4. X-ray diffraction patterns of the (**a**) CuO, (**b**) Si_P, (**c**) SCV_H, (**d**) SCV_{H+W} and (**e**) C-SCV_{H+W}.

Supplementary Fig. S3(a) and (b) online present the cyclic voltammetry curves of first and second cycle for SCV_{H+W}, C-SCV_{H+W} and Si_{H+W}, respectively in a voltage window of 0.005 to 2.0 V at a scan rate of 0.1 mV s^{-1}. Here, Si_{H+W}[23] is pure Si processed high mechanical milling and wet milling as the one of SCV_{H+W}. Accordingly, onset voltage of first cathodic curves is 0.36 V for SCV_{H+W} and 0.13 V for C-SCV_{H+W}, corresponding to observation of steep potential dropping for C-SCV_{H+W} as shown in Fig. 7(a). The different onset voltage in first cycle between SCV_{H+W} and C-SCV_{H+W} might be ascribed to glucose-derived carbon coated on surface of C-SCV_{H+W}, resulting in particular SEI formations. After SEI formation, onset voltage of second cathodic curves for C-SCV_{H+W} is started similar with SCV_{H+W} (Fig. S3(b)), consistent with observation in Fig. 7(b). Otherwise, the cathodic peaks around 0.23 V and 0.09 V could be attributed to the alloying reaction upon lithiation between Si and lithium, resulting in phase transformation of Li_xSi. The sharp anodic peak at around 0.09 V might be ascribed to the lithium stripping current from the lithium accumulation on surface of SCV_{H+W} during cathodic polarization. Two broad anodic peaks (0.29 and 0.47 V) can be attributed to the two-step delithiation of Li_xSi. In addition, we compare cyclic voltammetry between SCV_{H+W} and Si_{H+W}. The examination of the first lithiation scan of cyclic voltammetry (Fig. S3(a)), the onset voltage (0.36 V) and cathodic peaks (0.23 V, 0.09 V) for SCV_{H+W} present slightly shifting to higher voltage than Si_{H+W}, onset voltage (0.30 V) and cathodic peaks (0.20 V, 0.05 V). Moreover, the first delithiation scan shows that anodic peaks (0.47 V, 0.29 V) for SCV_{H+W} slightly shift to lower voltage than Si_{H+W}, anodic peaks (0.50 V, 0.33 V). This implies that the formation of Cu_3Si in pure Si could relatively enhances lithiation/delithiation kinetics.

Cycling tests of experimental electrodes conducted at 200 mA g^{-1} in a voltage range of 0.002–1.5 V (vs. Li$^+$/Li) in specific capacity is shown in Fig. 8(a). Initial capacity and retention capacity after 100 cycles are summarized in Table 2. Compared to SCV_H and SCV_{H+W}, suppression of fading for C-SCV_{H+W} within initial cycles could be contributed to residual carbon coated on surface as buffer space which leaving sufficient room for relaxing volume expansion between composite particles in lithiation/delithiation processes. Moreover, the construction of nanocrystalline Cu_3Si distributed in amorphous/nanocrystalline Si matrix is suspected to enhance the conductivity and strength inside the Si/Cu_3Si-based composite. Thus, the specific charge (delithiation) capacities of SCV_H, SCV_{H+W} and C-SCV_{H+W} after 100 cycles are 1022 mAh g^{-1}, 1317 mAh g^{-1} and 1224 mAh g^{-1}, corresponding to retention of 45.0%, 58.2% and 73.2%.

In order to investigate effects of active materials loading and current density on cycling performance for C-SCV_{H+W}, varied current density (100/200 mA g^{-1} in a voltage range of 0.002–1.5 V (vs. Li$^+$/Li)) and active materials loading (0.8/2.3 mg cm^{-2}) are examined in areal capacity variation. Results of initial areal capacity (delithiation) and retained capacity after 100 cycles are summarized in Table 3. Figure 8(b) presents the trend that C-SCV_{H+W} of lower loading (0.8 mg cm^{-2}) or lower conducted current density (100 mA g^{-1}) performs better relatively retained capacity. However, too low active materials loading means lower areal capacity to practical application in LIBs. To the optimum practice, coin cell made by C-SCV_{H+W} as negative electrode of active materials loading, 2.3 mg cm^{-2} conducted at 100 mA g^{-1} enables an initial charge (delithiation) capacity 1812 mAh g^{-1} (4.08 mAh cm^{-2}) with columbic efficiency of 83.7% and 1470 mAh g^{-1} (3.31 mAh cm^{-2}) at the end of the 100th cycle. Rate capabilities of SCV_H, SCV_{H+W} and C-SCV_{H+W} at current density 0.1, 0.2, 0.4, 1.0, 2.0, 4.0 then 0.2, 0.1 A g^{-1} between 0.002 V to 1.5 V are compared in Fig. 8(c). SCV_{H+W} and C-SCV_{H+W} exhibits better rate performance than SCV_H.

Samples	Si^0 (%)	Si^{1+} (%)	Si^{2+} (%)	Si^{3+} (%)	Si^{4+} (%)
Si$_P$	23.3	19.1	16.7	19.3	21.7
SCV$_H$	21.1	32.2	21.0	13.8	12.0
SCV$_{H+W}$	25.6	20.7	18.3	22.5	12.9
C-SCV$_{H+W}$	22.4	25.0	19.4	23.2	10.0

Table 1. Surface concentration measured by XPS deconvoluted by variety of oxidation states for Si2p spectra of Si$_P$, SCV$_H$, SCV$_{H+W}$ and C-SCV$_{H+W}$ powders.
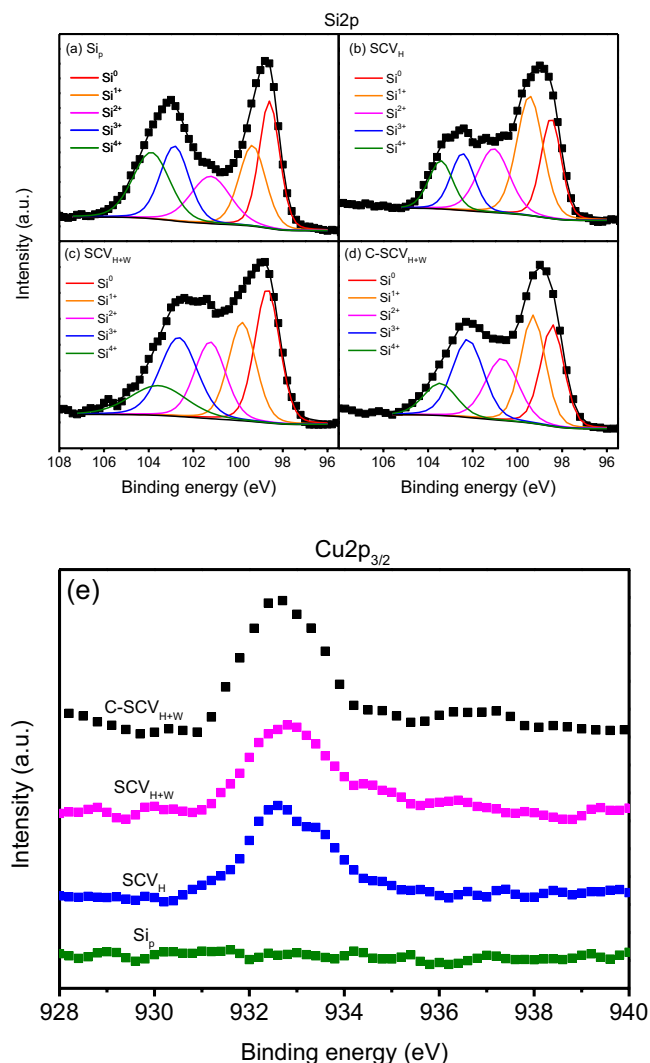

Figure 5. XPS spectra of the Si2p for (**a**) Si$_P$, (**b**) SCV$_H$, (**c**) SCV$_{H+W}$, (**d**) C-SCV$_{H+W}$ and (**e**) Cu2p$_{3/2}$ for Si$_P$, SCV$_H$, SCV$_{H+W}$ and C-SCV$_{H+W}$, respectively.

In addition, electrodes of blank Cu collector, pristine C-SCV$_{H+W}$ and 100th cycled C-SCV$_{H+W}$ are characterized by XRD in 2θ range from 42.5° to 48.0° as shown in Fig. S4. For pristine C-SCV$_{H+W}$ electrode (Fig. S4(b)), diffraction peak at 47.3° is attributed to the (220) for Si. In addition, diffraction peaks at 44.6°, 45.0° are attributed to the (012) and (300), respectively for Cu$_3$Si. After repeatedly lithiation/delithiation reactions, Si crystalline phase transforms into amorphous phase as shown in Fig. S4(c). In contrast, diffraction peaks of (012) and (300) for Cu$_3$Si are clearly observed after lithiation/delithiation process.

Discussion

In this work, the robust method to synthesize Si/Cu$_3$Si-based composite as negative electrode materials for lithium ion battery is disclosed. Our results reveal that high energy mechanical milling on Si/CuO mixture induces mechanochemical reaction, resulting in CuO decomposing, amorphizing and alloying with Si. In addition, Si is transformed from well crystalline structure to nanocrystalline/amorphous construction upon high energy
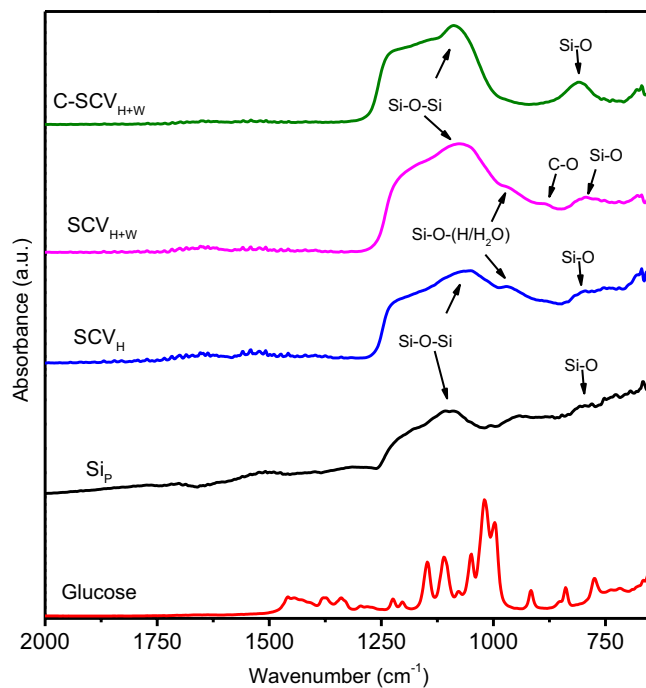
Figure 6. ATR-FTIR spectra for glucose, Si_P, SCV_H, SCV_{H+W} and C-SCV_{H+W}, respectively.
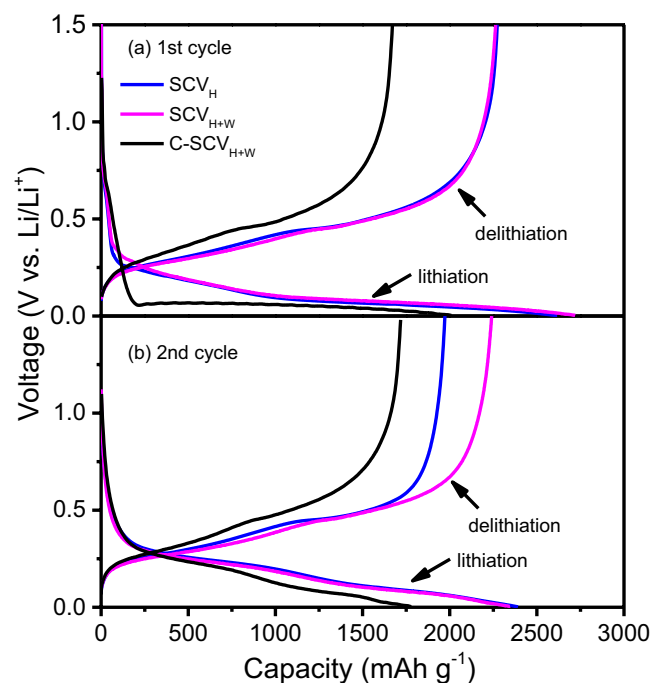
Figure 7. Voltage profiles of SCV_H, SCV_{H+W} and C-SCV_{H+W} for (**a**) 1st cycle and (**b**) 2nd cycle conducted at current density 200 mA g^{-1} between 0.002 V to 1.5 V.

impacting. Followed by carbonization, heating energy leads Cu_3Si to crystallizing and distributing in nanocrystalline/amorphous Si-rich matrix as rigid and conductive enhancer. Furthermore, residual carbon on surface of composite as buffer space alleviates the volume change upon lithiation/delithiation processes. Thus, coin cell made of C-coated Si/Cu_3Si-based composite (active materials loading, 2.3 mg cm^{-2}) as negative electrode conducted at 100 mA g^{-1} enables an initial charge capacity 1812 mAh g^{-1} (4.08 mAh cm^{-2}) with columbic efficiency of 83.7% and 1470 mAh g^{-1} (3.31 mAh cm^{-2}) at the end of the 100th cycle. Such a performance enables the Si/Cu_3Si-based composite as potential candidate for negative electrode materials for lithium ion battery.
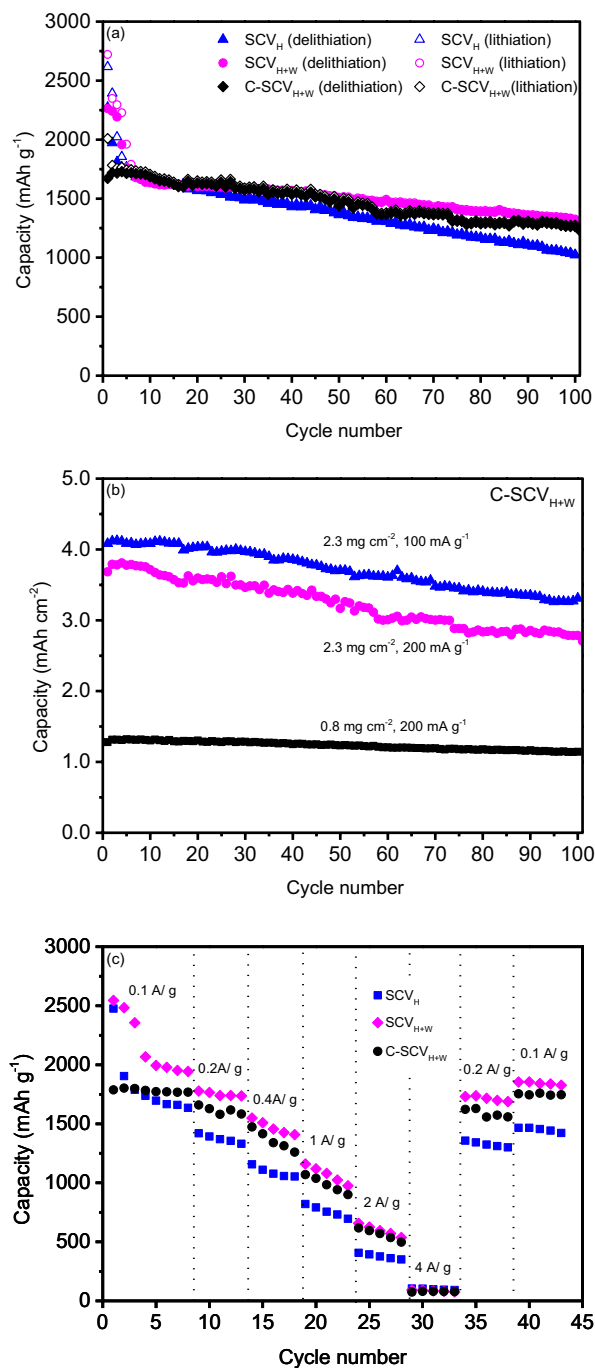
Figure 8. (**a**) Cycling performance of specific discharge (lithiation)/charge (delithiation) capacity for SCV_H, SCV_{H+W} and $C\text{-}SCV_{H+W}$ conducted at current density $200\,mA\,g^{-1}$ between $0.002\,V$ to $1.5\,V$. (**b**) Areal charge (delithiation) capacity comparison for $C\text{-}SCV_{H+W}$ of varied loading ($0.8/2.3\,mg\,cm^{-2}$) conducted at current density 100 and $200\,mA\,g^{-1}$ between $0.002\,V$ to $1.5\,V$. (**c**) Charge (delithiation) capability of SCV_H, SCV_{H+W} and $C\text{-}SCV_{H+W}$ at various charge and discharge rates conducted at current density 0.1, 0.2, 0.4, 1.0, 2.0, 4.0 then 0.2, $0.1\,A\,g^{-1}$ between $0.002\,V$ to $1.5\,V$.

Methods

Materials Preparation. Commercial silicon powder (Si_P, 99.9%, $10\,\mu m$, Fuzhou Hokin Chemical Technology, China), CuO powder (99.9%, 0.7 um, Nissin Chemco, Japan) and vapor grown carbon fiber (VGCF, Showa Denko K.K, Japan) were used as starting materials without further purifying. Si, CuO and VGCF powders were weighted stoichiometrically with weight ratio of 89: 10: 1. The mixture powder was loaded into stainless vial of 500 ml along with stain-less balls of 3 mm in dimension. The ball-to-powder mass ratio was 20:1. The vials were sealed under Ar atmosphere in the glove box. High energy mechanical milling (HEMM) was carried out at room temperature for 9 hours using a planetary miller (PM 400, Retsch, Germany) with a rotation speed of

Samples	1st discharge capacity (mAh g^{-1})	1st charge capacity (mAh g^{-1})	1st Columbic efficiency (%)	100th capacity (mAh g^{-1})	Retention (%)
SCV$_H$	2617	2273	86.9	1022	45.0
SCV$_{H+W}$	2722	2264	83.2	1317	58.2
C-SCV$_{H+W}$	2009	1671	83.2	1224	73.2

Table 2. Electrochemical properties of SCV$_H$, SCV$_{H+W}$ and C-SCV$_{H+W}$ conducted at 200 mA g^{-1} between 0.002 V to 1.5 V. The specific capacity was calculated based on the mass of active materials.

Loading (mg cm^{-2})	Current density (mAh g^{-1})	1st areal capacity (mAh cm^{-2})	100th areal capacity (mAh cm^{-2})	Retention (%)
0.8	200	1.28	1.14	89.1
2.3	100	4.08	3.31	81.1
2.3	200	3.68	2.69	73.1

Table 3. Effects of active materials loading and current density on areal capacity (delithiation) performance for C-SCV$_{H+W}$ conducted between 0.002 V to 1.5 V.

300 rpm. The milled mixture was denoted as SCV$_H$ (micro-sized aggregate). Then, SCV$_H$ is introduced into polypropylene jar along with ZrO$_2$ balls of 2 mm dimension and ethanol medium. The ball-to-powder mass ratio was 10:1. The wet milling was carried out at room temperature using a rotation mixer at 250 rpm. After wet milling, powder was filtered and dried at 120 °C in vacuum for 12 hours. The wet milled SCV$_H$ was denoted as SCV$_{H+W}$ (submicro-sized aggregate). Particle size distribution at 50%, D50 for SCV$_{H+W}$ was controlled around 0.4 μm. Meanwhile, SCV$_{H+W}$ was mixed with glucose (weight ratio 1: 0.4) in ethanol then dried at 120 °C in vacuum for 12 hours. The dried mixture of SCV$_{H+W}$/glucose was placed in an alumina crucible, followed by loading into the alumina tube furnace. The temperature was increased to 800 °C at heating rate 10 °C min^{-1} and held for 1 hour under a mixture gas flow of argon (150 ml min^{-1}), hydrogen (20 ml min^{-1}). Then, the furnace was nature cooled, while the argon gas (150 ml min^{-1}) was continuously flushed through the alumina tube until to room temperature. The carbonization of glucose modified SCV$_{H+W}$ was denoted as C- SCV$_{H+W}$.

Characterization. The morphology was observed by field emission scanning electron microscope (Carl Zeiss AURIGA CrossBeam (FIB-SEM) Workstation) using an accelerating voltage of 5 kV and high-resolution transmission electron microscope (HRTEM, JEM-2100F, JEOL) with an accelerating voltage of 200 kV. Si composite powders were dispersed in ethanol, and then transferred onto a Formvar carbon coated nickel grid for TEM sample preparation.

The crystal structure was characterized by X-ray diffractometer (D8 ADVANCE Eco) with Cu Kα radiation (λ = 0.15418 nm). Particle size distribution was determined by the laser scattering method using a laser diffraction particle size analyzer (Horiba LA960). Chemical surface composition analysis of the Si powders was conducted using X-ray photoelectron spectroscopy (XPS, PHI 5000 VersaProbe) equipped with an Al Kα X-ray radiation source operating at 1486.6 eV. All spectra were calibrated using C (sp^2) as a reference binding energy of 284.6 eV. Thermogravimetric analysis (TGA) was carried out using thermogravimetric analyzer (TA Instruments, USA) from 25 °C to 800 °C with a heating rate of 10 °C min^{-1} under air atmosphere. Fourier transform infrared (FTIR) measurement of the Si powders was performed on attenuated total reflectance (ATR) mode using a Cary 660 (Agilent Technologies) FT-IR system equipped with an MCT detector. All spectra were scanned from 650 cm^{-1} to 2000 cm^{-1} with resolution of 2 cm^{-1} for 256 scans.

Electrochemical Measurements. The slurry was prepared by combining the solid components as 65 wt% of SCV$_H$, SCV$_{H+W}$ and C-SCV$_{H+W}$, respectively, 20 wt% of Super P (MMM Carbon, Blegium), 9 wt% of poly(acrylic acid) (PAA, Sigma-Aldrich Co.), 2.5 wt% of carboxymethyl cellulose (CMC, Sigma-Aldrich Co.) and 3.5 wt% of styrene butadiene rubber (SBR, Zeon Co.) in deionized water. Mixing was carried out by a planetary mixer (G-Mixer 400 S, Gold Max Applied Materials Co.) at 500 rpm for 60 min. Electrodes were prepared by casting the slurry onto a sheet of copper foil (Nippon Foil Co.) and dried in the oven at 90 °C for 1 hour. The anodes were stored in a glove box (with oxygen and humidity content maintained below 10 ppm) for more than 24 hours before electrochemical testing. The 2032 coin-type cells were assembled, consisting of a test electrode, lithium foil as a counter electrode and a glass fiber separator (GA-100, Advantec) in an Ar-filled glove box. Electrolyte solution was 1 M LiPF$_6$ in a mixture of ethylene carbonate (EC, Ferro Co.), dimethyl carbonate (DMC, Ferro Co.) (1:1 by weight) and additive of 10 wt% fluorinated ethylene carbonate (FEC, Sigma-Aldrich Co.). For the cycle test, the cells were conducted in galvanostatic discharge (lithiation)/charge (delithiation) tests between 0.002 and 1.5 V versus Li$^+$/Li using a multi-channel battery testing system (AcuTech Sys-tems BAT-750B). The specific capacity was calculated based on the mass of active materials. Cyclic voltammetry (CV) measurement was carried out using an Autolab electrochemical analyzer (Autolab PGSTAT30, Eco Chemie) with scan rate of 0.1 mV s^{-1} and a potential range of 0.005–2 V (vs. Li$^+$/Li). All electrochemical tests were performed at 25 °C.

References

1. Larcher, D. & Tarascon, J. M. Towards greener and more sustainable batteries for electrical energy storage. *Nat. Chem.* **7**, 19 (2014).
2. Choi, J. W. & Aurbach, D. Promise and reality of post-lithium-ion batteries with high energy densities. *Nat. Rev. Mater.* **1**, 16013 (2016).
3. Liu, J. *et al.* Materials Science and Materials Chemistry for Large Scale Electrochemical Energy Storage: From Transportation to Electrical Grid. *Adv. Funct. Mater.* **23**, 929–946 (2013).
4. Boukamp, B. A., Lesh, G. C. & Huggins, R. A. All-Solid Lithium Electrodes with Mixed-Conductor Matrix. *J. Electrochem. Soc.* **128**, 725–729 (1981).
5. Kasavajjula, U., Wang, C. S. & Appleby, A. J. Nano- and bulk-silicon-based insertion anodes for lithium-ion secondary cells. *J. Power Sources* **163**, 1003–1039 (2007).
6. Liu, X. H. *et al.* Size-dependent fracture of silicon nanoparticles during lithiation. *ACS Nano* **6**, 1522–1531 (2012).
7. Chan, C. K. *et al.* High-performance lithium battery anodes using silicon nanowires. *Nat. Nanotech.* **3**, 31–35 (2008).
8. Ge, M. Y. *et al.* Large-Scale Fabrication, 3D Tomography, and Lithium-Ion Battery Application of Porous Silicon. *Nano Lett.* **14**, 261–268 (2014).
9. Kim, I. S. & Kumta, P. N. High capacity Si/C nanocomposite anodes for Li-ion batteries. *J. Power Sources* **136**, 145–149 (2004).
10. Kim, J.-H., Kim, H. & Sohn, H.-J. Addition of Cu for carbon coated Si-based composites as anode materials for lithium-ion batteries. *Electrochem. Commun.* **7**, 557–561 (2005).
11. Hwang, T. H., Lee, Y. M., Kong, B. S., Seo, J. S. & Choi, J. W. Electrospun Core-Shell Fibers for Robust Silicon Nanoparticle-Based Lithium Ion Battery Anodes. *Nano Lett.* **12**, 802–807 (2012).
12. Pan, L. *et al.* Facile synthesis of yolk-shell structured Si-C nanocomposites as anodes for lithium-ion batteries. *Chem. Commun.* **50**, 5878–5880 (2014).
13. Schroder, K. *et al.* The Effect of Fluoroethylene Carbonate as an Additive on the Solid Electrolyte Interphase on Silicon Lithium-Ion Electrodes. *Chem. Mater.* **27**, 5531–5542 (2015).
14. Magasinski, A. *et al.* Toward Efficient Binders for Li-Ion Battery Si-Based Anodes: Polyacrylic Acid. *ACS Appl. Mater. Interfaces* **2**, 3004–3010 (2010).
15. Zhou, J. *et al.* $Cu_3Si@Si$ core-shell nanoparticles synthesized using a solid-state reaction and their performance as anode materials for lithium ion batteries. *Nanoscale* **7**, 15075–15079 (2015).
16. Shimoi, N., Qiwu, Z., Bahena-Garrido, S. & Tanaka, Y. Mechanochemical approaches to employ silicon as a lithium-ion battery anode. *AIP Adv.* **5**, 057142 (2015).
17. Du, Z. *et al.* Electrochemistry of Cu_xSi_{1-x} Alloys in Li Cells. *J. Electrochem. Soc.* **163**, A1275–A1279 (2016).
18. Cheng, Y. *et al.* Influence of copper addition for silicon-carbon composite as anode materials for lithium ion batteries. *RSC Adv.* **6**, 56756–56764 (2016).
19. Kim, S.-O. & Manthiram, A. Low-cost carbon-coated Si-Cu_3Si-Al_2O_3 nanocomposite anodes for high-performance lithium-ion batteries. *J. Power Sources* **332**, 222–229 (2016).
20. Woo, J.-Y. *et al.* Cu_3Si-doped porous-silicon particles prepared by simplified chemical vapor deposition method as anode material for high-rate and long-cycle lithium-ion batteries. *J. Alloys Compd.* **701**, 425–432 (2017).
21. Deng, L. *et al.* Facile synthesis of N-doped carbon-coated Si/Cu alloy with enhanced cyclic performance for lithium ion batteries. *RSC Adv.* **6**, 78100–78105 (2016).
22. Suryanarayana, C. Mechanical alloying and milling. *Prog. Mater. Sci.* **46**, 1–184 (2001).
23. Hou, S.-C. *et al.* The synergistic effects of combining the high energy mechanical milling and wet milling on Si negative electrode materials for lithium ion battery. *J. Power Sources* **349**, 111–120 (2017).
24. Yubero, F., Barranco, A., Mejias, J. A., Espinos, J. P. & Gonzalez-Elipe, A. R. Spectroscopic characterisation and chemical reactivity of silicon monoxide layers deposited on Cu(100). *Surf. Sci.* **458**, 229–238 (2000).
25. Wang, D., Gao, M., Pan, H., Wang, J. & Liu, Y. High performance amorphous-$Si@SiO_x$/C composite anode materials for Li-ion batteries derived from ball-milling and *in situ* carbonization. *J. Power Sources* **256**, 190–199 (2014).
26. Dahlang, T. & Sven, T. Electronic and optical properties of Cu, CuO and Cu_2O studied by electron spectroscopy. *J. Phys.: Condens. Matter* **24**, 175002 (2012).
27. V., H., A., F., A., H. & H., T. XPS study of the atmospheric corrosion of copper alloys of archaeological interest. *Surf. Interface Anal.* **36**, 876–879 (2004).
28. Shengqi, X., Jingen, Z., Xiaotian, W. & Dongwen, Z. The reduction of CuO by Si during ball milling. *J. Mater. Sci. Lett.* **15**, 634–635 (1996).
29. Chromik, R. R., Neils, W. K. & Cotts, E. J. Thermodynamic and kinetic study of solid state reactions in the Cu–Si system. *J. Appl. Phys.* **86**, 4273–4281 (1999).
30. Liu, Z. *et al.* Silica-Derived Hydrophobic Colloidal Nano-Si for Lithium-Ion Batteries. *ACS Nano* **11**, 6065–6073 (2017).
31. Wei, L. M., Chen, C. X., Hou, Z. Y. & Wei, H. Poly (acrylic acid sodium) grafted carboxymethyl cellulose as a high performance polymer binder for silicon anode in lithium ion batteries. *Sci. Rep.* **6** (2016).
32. Li, M. *et al.* Nanosilica/carbon composite spheres as anodes in Li-ion batteries with excellent cycle stability. *J. Mater. Chem. A* **3**, 1476–1482 (2015).
33. Rahman, I. A., Vejayakumaran, P., Sipaut, C. S., Ismail, J. & Chee, C. K. Size-dependent physicochemical and optical properties of silica nanoparticles. *Mater. Chem. Phys.* **114**, 328–332 (2009).

Acknowledgements

Author Contributions

J.-L.H. and C.-C.C. managed and coordinated the research teams. S.-C.H. designed the experiments and wrote the manuscript. Y.-H.W. and H.-Y.C. conducted the synthesis experiments and analyzed the composite powders. X.-D.L. and Y.-Q.C. prepared the testing cells and performed the electrochemical measurements. T.-Y.C. helped in data analysis and manuscript writing. All the authors participated in discussions of the results

Additional Information

Supplementary information accompanies this paper at https://doi.org/10.1038/s41598-018-30703-3.

Competing Interests: The authors declare no competing interests.

Publisher's note: Springer Nature remains neutral with regard to jurisdictional claims in published maps and institutional affiliations.